


## Article

# One Convenient Method to Calculate Performance and Optimize Configuration for Annular Radiator Using Heat Transfer Unit Simulation

Zhe Xu <sup>1,2,\*</sup>, Yingqing Guo <sup>1</sup> , Huarui Yang <sup>2</sup>, Haotian Mao <sup>1</sup>, Zongling Yu <sup>2</sup> and Rui Li <sup>2</sup>

<sup>1</sup> School of Power and Energy, Northwestern Polytechnical University, Xi'an 710129, China; yqguo@nwpu.edu.cn (Y.G.); alexmao@mail.nwpu.edu.cn (H.M.)

<sup>2</sup> Xinxiang Aviation Industry (Group) Co., LTD., AVIC, Xinxiang 453049, China; hryangxh@163.com (H.Y.); zonglingy@163.com (Z.Y.); ruiliixh@163.com (R.L.)

\* Correspondence: zhexu@mail.nwpu.edu.cn

Received: 4 December 2019; Accepted: 3 January 2020; Published: 5 January 2020



**Abstract:** In order to calculate heat transfer capacity and air-side pressure drop of an annular radiator (AR), one performance calculation method was proposed combining heat transfer unit (HTU) simulation and plate-and-fin heat exchanger (PFHX) performance calculation formulas. This method can obtain performance data with no need for meshing AR as a whole, which can be convenient and time-saving, as grid number is reduced in this way. It demonstrates the feasibility of this performance calculation method for engineering applications. In addition, based on the performance calculation method, one configuration optimization method for AR using nondominated sorted genetic algorithm-II (NSGA-II) was also proposed. Fin height (FH) and number of fins in circumferential direction (NFCD) were optimized to maximize heat transfer capacity and minimize air-side pressure drop. Three optimal configurations were obtained from the Pareto optimal points. The heat transfer capacity of the optimal configurations increased by 22.65% on average compared with the original configuration, while the air-side pressure drop decreased by 33.99% on average. It indicates that this configuration optimization method is valid and can provide a significant guidance for AR design.

**Keywords:** annular radiator; performance calculation; configuration optimization; heat transfer unit; plate-and-fin heat exchanger; nondominated sorted genetic algorithm-II

## 1. Introduction

Heat exchangers, which can transfer heat between two fluids of different temperatures, are widely used in several industrial applications, just like aerospace engineering, petrochemical progress, nuclear power plants, oil refining, and so on [1]. As performance calculation and configuration optimization are main steps in the process of heat exchanger design, numerous up-to-date technologies have been applied in this research area from various points of view.

Theoretical analysis is a common method to calculate heat exchanger performance. As one kind of well-known theoretical analysis method, the Bell–Delaware method is widely used in performance calculation of heat exchangers. In the research of L. Yi et al. [2], one cooling water heat exchanger was designed preliminarily using the Bell–Delaware method, and the design results were verified by HTRI 6.0 commercial software. Some mathematical relationship formulas for performance calculation of shell-and-tube heat exchanger (STHX) with helical baffles were proposed by B. A. Abdelkader et al. [3] based on Bell–Delaware method. In addition, in the research of B. A. Abdelkader et al. [4], Kern method, Bell–Delaware method, and flow stream analysis (Wills Johnston) methods were applied, respectively, to predict both heat-transfer coefficient and pressure drop on the shell side of a heat exchanger.

The calculation results were compared with the experimental data, and the comparison results showed that the Bell–Delaware method was the most accurate method.

Computational fluid dynamics (CFD) technology is also widely used in performance analysis of heat exchangers. The performances of STHXs with and without baffles were compared through CFD calculation program OpenFOAM-2.2.0 by E. Pal et al. [5]. In the research of J. Du et al. [6], a midtemperature gravity heat pipe exchanger was taken as the research object, and the effects of different operating parameters and fin parameters on heat transfer performance were studied using Fluent software. A multitube tank was proposed by M. Ramadan et al. [7] as a heat exchanger. The performance of it was analyzed using CFD simulation code, and the best scenario among three different configurations was obtained by an optimization procedure. Y. Yang et al. [8] studied heat transfer and flow characteristics in a type of plate heat exchanger by numerical simulation, and the correlations of single-phase heat transfer coefficient and friction coefficient were presented. In the research of plate-and-fin heat exchangers (PFHXs), the effects of inlet header configuration on fluid flow maldistribution and the effects of top bypass flow of fins on thermal performance were studied by A. Raul et al. [9] and H. Cai et al. [10] using CFD simulation, respectively. In addition, based on CFD technology, the performances of STHXs separately with segmental baffles [11,12], trefoil-hole baffles [12,13], and helical baffles [11,12,14] were analyzed. Especially in the research of A. El Maakoul et al. [12], the simulation results of these three kinds of heat exchangers were compared, and STHX with helical baffles was found to be the one that had the best comprehensive performance.

Combining theoretical analysis with CFD simulation can be another useful way to research heat exchanger performance. R. Amini et al. [15] compared the CFD simulation results with the calculation results by the Bell–Delaware method to validate the accuracy of the simulation method. D.M. Godino et al. [16] calculated the heat transfer coefficient of the preheater separately by Bell–Delaware method and Kern method, and the calculation results were both compared with the CFD simulation data to analyze the accuracy. X. Gu et al. [17] came up with periodic whole cross-section computation models to obtain performance data of segmental baffle heat exchanger, shutter baffle heat exchanger, and trapezoid-like tilted baffle heat exchanger, and the reliability of the method was verified by comparing the simulation data with the calculation results using the Bell–Delaware method. I. Milcheva et al. [18] improved the traditional Bell–Delaware method and introduced an enhancement factor to calculate the performance of a STHX with double-segmental baffles. The calculation results were compared with the CFD simulation data to validate the effectiveness of this method.

As for configuration optimization for heat exchanger, nondominated sorted genetic algorithm-II (NSGA-II) is commonly used in some research. The Bell–Delaware procedure and the  $\varepsilon$ -NTU method were applied in STHX performance estimation by S. Sanaye et al. [19] and NSGA-II was used to maximize heat transfer coefficient and minimize pressure drop simultaneously. M. Chahartaghi et al. [20] combined NSGA-II with entransy dissipation theory to minimize the entransy dissipation numbers separately caused by thermal conduction and fluid friction for STHX. Z. Xu et al. [21] calculated the performances of two kinds of STHXs by theoretical formulas and optimized their structural parameters using NSGA-II, respectively. In order to optimize the configuration of a PFHX with offset strip fins, NSGA-II combined with the  $\varepsilon$ -NTU method was adopted in the research of R. Song et al. [22]. In addition, as a popular optimization method, NSGA-II combined with response surface method was also used in the configuration optimizations of STHX with helical baffles [23–25], spiral-wound heat exchanger [26], helically coiled tube heat exchanger [27], torsional flow heat exchanger [28], and triple concentric-tube heat exchanger [29]. Except for NSGA-II, some other novel optimization algorithms were also proposed to optimize configuration parameters of different heat exchangers, such as firefly algorithm [30], Tsallis differential evolution algorithm [31], bat algorithm [32], Taguchi method [33], particle swarm optimization (PSO) [34], cohort intelligence algorithm [35], tree traversal method [36], surrogate-based optimization algorithm [37], wale optimization [38], topology optimization [39], Jaya algorithm [40], and so on.

As annular radiator (AR) is a neoteric heat exchanger, the research about its thermal-hydraulic performance calculation and configuration optimization, which are badly in need of design processes, are rare. In this paper, a feasible and reliable method for performance calculation and configuration optimization based on heat transfer unit (HTU) simulation and NSGA-II was proposed, which can conveniently obtain AR heat transfer capacity and air-side pressure drop, while avoiding the problem of the huge amount of grids generated by meshing AR as a whole directly, and getting the optimized fin height (FH) and number of fins in circumferential direction (NFCD), which are a trade-off on maximizing heat transfer capacity and minimizing air-side pressure drop.

## 2. Method

### 2.1. Physical Model and Normal Operating Conditions

AR is an air–liquid heat exchanger, which mainly consists of liquid channels, annular substrate, and fins. As depicted in Figure 1, liquid flows through the channels inside the annular substrate, and air passes by the fins, which are averagely distributed on the circular inner side of the annular substrate. So, the heat can be transferred from the liquid of higher temperature to the air of lower temperature through fins and annular substrates.

The material of AR is aluminum alloy, and the normal operating conditions are shown in Table 1. In this case, the working fluid of liquid is lubricating oil.

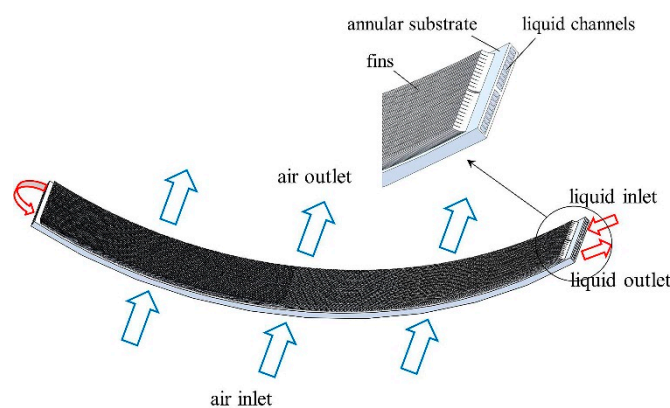


Figure 1. Schematic diagram of annular radiator (AR).

Table 1. Normal operating conditions of AR.

Normal Operating Condition	Value
Liquid inlet volume flow rate (L/min)	30
Liquid inlet temperature (K)	423
Air inlet mass flow rate (kg/h)	5500
Air inlet temperature (K)	286
Air inlet pressure (kPa)	5.1

### 2.2. Performance Calculation Method

#### 2.2.1. Structural Equivalence

As AR is structurally similar to PFHX with fins of rectangular straight wave, the performance calculation formulas of this kind of heat exchanger were applied to the calculation of AR heat transfer capacity in this method. Basic formulas of PFHX heat transfer capacity calculation are given in Appendix A. The structure of the equivalent PFHX is depicted in Figure 2. The main configuration parameters of AR and the corresponding PFHX are shown in Figure 3 and Table 2.

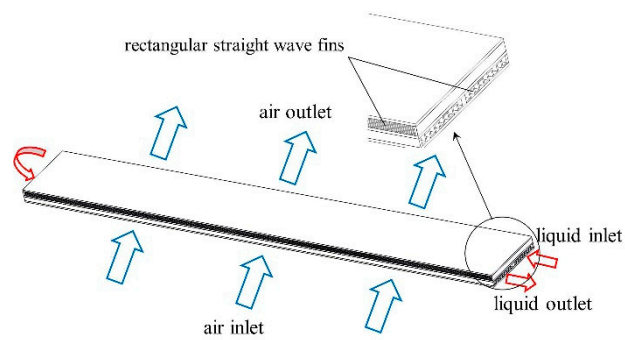


Figure 2. Structure of the equivalent plate-and-fin heat exchanger (PFHX).

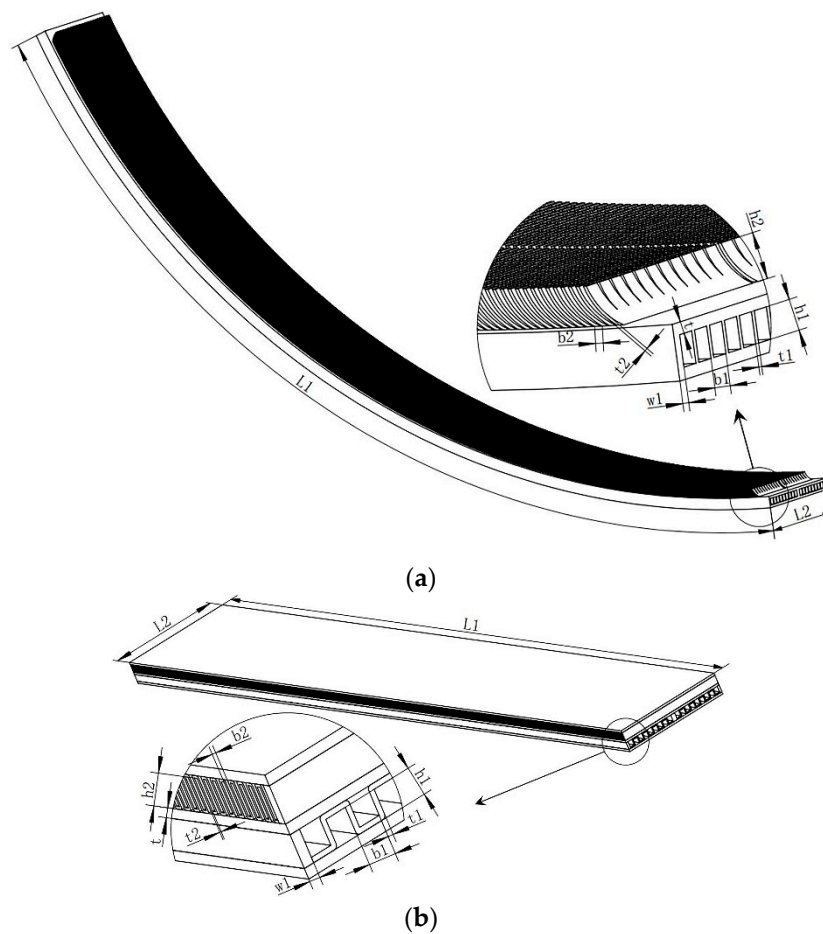


Figure 3. Configuration parameter correspondence between AR and PFHX: (a) configuration parameters of AR; (b) corresponding configuration parameters of PFHX.

Table 2. Configuration parameter values.

Configuration Parameter	Value (mm)	Configuration Parameter	Value (mm)
L1	1185	L2	150
b1	7.8	b2	2.1
h1	8	h2	10
t1	1.5	t2	0.8
w1	3	t	3



### 2.2.2. HTU Simulation Method

A traditional way to obtain the performance data of a heat exchanger is through emulating it as a whole directly. While, for AR simulation, a huge number of grids will be generated by this traditional method in the process of meshing. That is extremely time-consuming for solving and is beyond the available computing resources. In order to avoid this problem, HTU simulation, rather than overall simulation of AR, was used in this method. When an AR is working, the air above the fins of the AR does not pass through the clearance between fins, which means that it is unscientific if the air inlet flow rate of AR is used in the PFHX performance calculation formulas directly. So, the percentage of the air calculated in the formulas needs to be obtained through HTU simulation in this method. This percentage is defined by Equation (1):

$$k = q_{fin} / q_{HTU}. \quad (1)$$

In Equation (1),  $q_{fin}$  and  $q_{HTU}$  are the volume flow rates of the air passing through the clearance between fins of HTU and the air of HTU air-side, respectively, and  $k$  reflects the percentage of the air that can be calculated in PFHX performance calculation formulas.

HTUs are obtained through dividing AR, and two kinds of HTUs can be obtained according to the symmetry of AR, as shown in Figure 4. As HTU A and HTU B are structurally similar, and air flows through HTU A first, HTU A was chosen to be the only one kind of HTU to be emulated in this method. In this case, the central angle of HTU was 2 degrees.

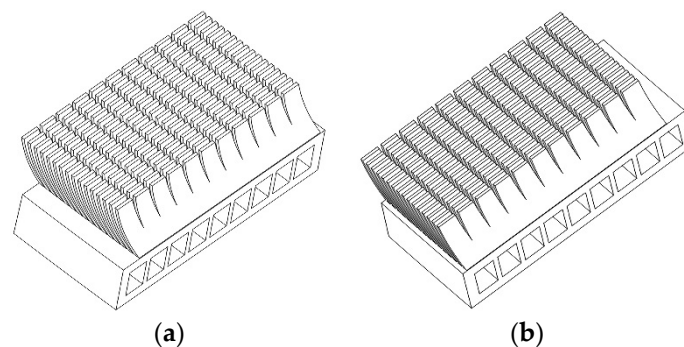


Figure 4. Two kinds of heat transfer units (HTUs): (a) HTU A; (b) HTU B.

In the process of CFD simulation, ANSYS commercial software was adopted. There were two fluid domains, including air domain and liquid domain, and one solid domain in the CFD simulation of HTU, as shown in Figure 5. Unstructured grids were adopted, and the normal operating conditions of AR were used in HTU simulation. In order to improve simulation accuracy, grid independence validation was carried out. In Figure 6,  $\Delta P'$  represents air-side pressure drop of HTU. As shown in this figure, the simulation deviations of  $k$  and  $\Delta P'$  were both in the acceptable range when the grid number increases above the point of 24,020,699. So, the mesh generation settings of this point were used.

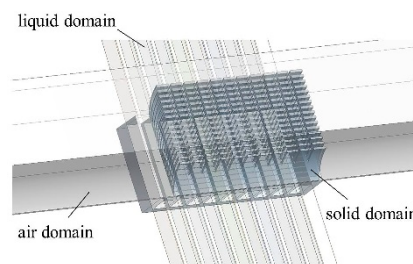


Figure 5. HTU computational domains.

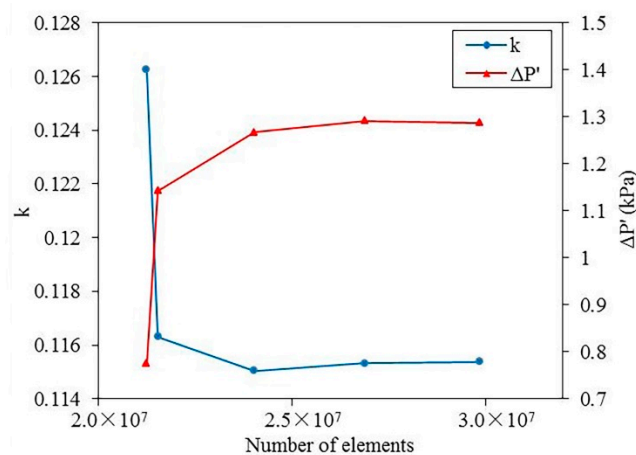


Figure 6. Grid independence validation.

In this case, the air flow rate was less than Ma0.3, and the temperature deviation between air inlet and outlet was small. So, like liquid, air was treated as a Newtonian and incompressible fluid with constant physical property parameters. In addition, in the process of simulation, fluid flow and heat transfer process were considered as turbulent and in steady-state, and fouling resistance was neglected.

In this method, a realizable  $k$ - $\varepsilon$  turbulence model and the default constant values were adopted. Velocity-inlet and pressure-outlet were separately used as inlets and outlets of both air and liquid. In the process of solving this kind of fluid flow heat transfer problem, the SIMPLE (semi-implicit method for pressure-linked equations) algorithm is the most widely used. The core of the algorithm is to use continuous equations and momentum equations to construct an approximate pressure correction equation on staggered grids to calculate pressure field and correct velocity. The SIMPLE algorithm is very useful in engineering applications. However, the convergence velocity of the SIMPLE algorithm is not fast. Compared with the SIMPLE algorithm, the SIMPLEC (SIMPLE-consistent) algorithm, which is the improved version of SIMPLE algorithm, can achieve a higher rate of convergence as it synchronizes speed field improvement process with pressure field improvement process [41]. Thus, in this study, SIMPLEC algorithm, as one built-in solution algorithm in ANSYS Fluent commercial software, was chosen to solve the simulation problem. The second order upwind was used for the momentum, turbulent kinetic energy, turbulent dissipation rate, and energy. The default convergence criterion was adopted, which is that the normalized residuals are less than  $1 \times 10^{-6}$  for energy equation and  $1 \times 10^{-3}$  for the other equations. Iteration number was set as 2000.

### 2.2.3. Method Procedure

AR performance calculation in this method included heat transfer capacity calculation and air-side pressure drop calculation. The main procedures are shown as follows:

1. Input the configuration parameters of AR as shown in Figure 3 and Table 2, and input the normal operating conditions of AR shown in Table 1.
2. Obtain HTU through dividing AR, and emulate HTU under the normal operating conditions of AR.
3. According to HTU simulation results, acquire  $k$  and  $\Delta P'$ .
4. Calculate the air inlet volume flow rate of AR, which can be used in PFHX performance calculation formulas by Equation (2):

$$q_v = kq_v' \quad (2)$$

In Equation (2),  $q_v$  is the air inlet volume flow rate of AR used in PFHX performance calculation formulas and  $q_v'$  is the air inlet volume flow rate of AR.

5. Calculate air-side pressure drop of AR. As HTU is obtained by cutting AR along its symmetry plane, air-side pressure drop of AR can be computed by Equation (3):

$$\Delta P = 2\Delta P' \quad (3)$$

In Equation (3),  $\Delta P$  is air-side pressure drop of AR.

6. Calculate heat transfer capacity of AR using PFHX performance calculation formulas.
  - (a) Assume one heat transfer capacity for AR.
  - (b) Calculate the mean temperature of liquid/air-side under the assumptive heat transfer capacity.
  - (c) Calculate the physical property parameters (such as fluid density, kinematic viscosity, etc.) of liquid/air-side under the mean temperature of the corresponding side.
  - (d) Calculate the effective heat transfer area values and the heat transfer coefficients of liquid-side and air-side.
  - (e) Calculate NTU (number of transfer units), heat transfer efficiency, and heat transfer capacity.
  - (f) Give the value of the calculated heat transfer capacity to the assumptive heat transfer capacity, and go to step (b) until the deviation of them is within acceptable limits.
  - (g) Output the calculated heat transfer capacity.

The flowchart of this method is shown in Figure 7.

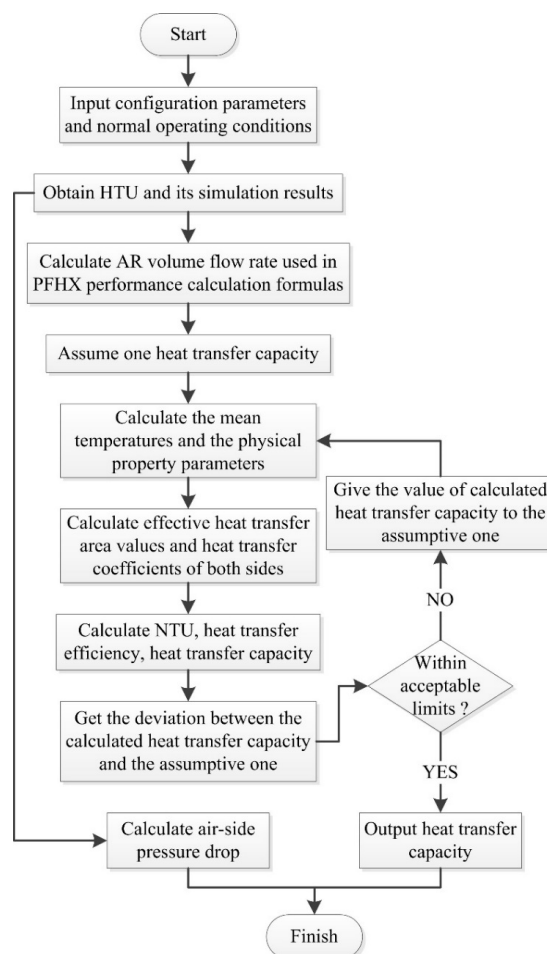


Figure 7. Flowchart of AR performance calculation method.

### 2.3. Configuration Optimization Method

In this research, in consideration of the performances of AR, heat transfer capacity  $Q$  and air-side pressure drop  $\Delta P$  were chosen as two objective functions, and FH and NFCD were regarded as two design parameters. Thus, the multiobjective optimization problem was formulated as Equation (4):

$$\begin{cases} \text{Min} & -Q, \Delta P \\ \text{S.t.} & 7\text{mm} \leq FH \leq 16\text{mm} \& FH \in Z \\ & 238 \leq NFCD \leq 544 \& NFCD \in Z \end{cases} \quad (4)$$

For a multiobjective optimization problem, it is always hard to find a solution that is absolutely optimal. However, through some evolutionary algorithms, a Pareto optimal front that contains a series of optimal solutions can be obtained. NSGA-II is one kind of evolutionary algorithm that is based on a genetic algorithm for multiobjective optimization. One or more satisfactory solutions can be selected by some criteria from the Pareto optimal front obtained by NSGA-II [24]. It incorporates elitism [42], and no sharing parameter needs to be chosen a priori [43]. As the nondominated sorting method is used as the ranking scheme in this algorithm, the convergence velocity of NSGA-II is faster than the traditional Pareto ranking method. Besides, as the constraint handling method also uses a nondominance principle as the objective, which guarantees that the feasible solutions are always ranked higher than the unfeasible solutions, penalty functions and Lagrange multipliers are not needed in NSGA-II [44]. So, due to these advantages, and in order to optimize these two configuration parameters shown in Equation (4) under the normal operating conditions shown in Table 1, the multiobjective genetic algorithm NSGA-II is adopted in this configuration optimization method to obtain the optimal solutions. The main procedures are shown as follows:

1. The two design parameters and the constraints of them, and the two conflicting optimization objectives are initialized.
2. Emulate HTUs of some different values of the two design parameters and record the corresponding simulation data of  $k$  and  $\Delta P'$ .
3. Obtain the functional relationships shown in Equations (5) and (6) by fitting using the simulation data calculated in step 2.

$$k = f_1(FH, NFCD), \quad (5)$$

$$\Delta P' = f_2(FH, NFCD) \quad (6)$$

4. Optimize design parameters using NSGA-II based on the AR performance calculation method in this research and the functional relationships obtained in step 3.
  - (a) Initialize NSGA-II parameters, including population size, generation number, and so on, and generate a random population in the constraints of design parameters.
  - (b) Calculate objective function values for each chromosome of the population using AR performance calculation method and the functional relationships obtained in step 3.
  - (c) Sort chromosomes based on non-domination and crowding distance. In this method, the crowding distance is compared only if the ranks for both chromosomes are the same.
  - (d) Choose the chromosomes that are fit for reproduction as the parents of the next generation using tournament algorithm.
  - (e) Generate children by crossover and mutation, and calculate their objective function values using AR performance calculation method and the functional relationships obtained in step 3.
  - (f) Combine parents and children, and sort them based on nondomination and crowding distance.
  - (g) A new generation is extracted based on ranking.

- (h) The above procedures are repeated from step (d) until convergence.
- (i) Output the Pareto optimal front which consists of a series of solutions.

Other details of NSGA-II are referred in [43]. The flowchart of this method is shown in Figure 8.

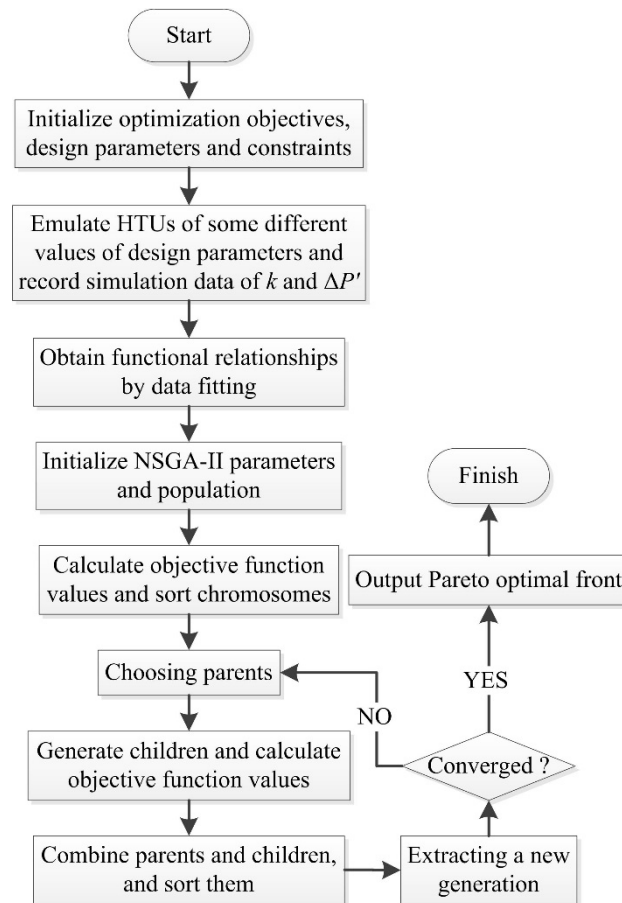


Figure 8. Flowchart of AR configuration optimization method.

### 3. Results and Discussion

#### 3.1. Performance Calculation Method Validation

HTU simulation results are shown in Figure 9. As depicted, when air passes by fins, only a small part of air passes through the clearance between fins, and the velocity of the air goes above fins is higher than that of the other. So, the calculation of  $k$  is significant. Based on the plane perpendicular to the air flow direction and located in the middle place of the finned area, the calculated  $k$  was 11.5%. That means only 11.5% of the air passes through the clearance between fins and can be used in PFHX performance calculation formulas.

In order to validate the accuracy of the AR performance calculation method, the calculation results were compared with the experimental data. The experimental conditions, the experimental schematic diagram, and the testing equipment for AR are shown in Table 1 and Figure 10; Figure 11, respectively. The experimental equipment included an air supply system, oil circulation system, and measuring system. An air supply system can provide AR the airflow of the required flow rate, temperature, and pressure. The maximum air supply capacity of it is 8600 kg/h, which can meet the requirement of this test. An oil circulation system can heat the lubricating oil to the required temperature and then supply it to AR. The measuring system includes some instruments distributed in the inlets and outlets of both air and oil. As the radius of AR is large, five pressure sensors and five temperature

sensors were averagely distributed in the air inlet of AR, and the same is true for the air outlet. The experimental temperature or pressure value of the air inlet or outlet of AR was computed by averaging the corresponding five measured values. The results of the comparison between calculation results and experimental data are given in Figure 12.

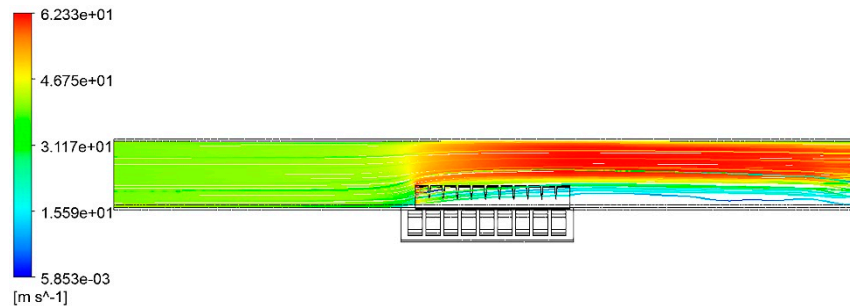


Figure 9. Velocity streamline of HTU air-side.

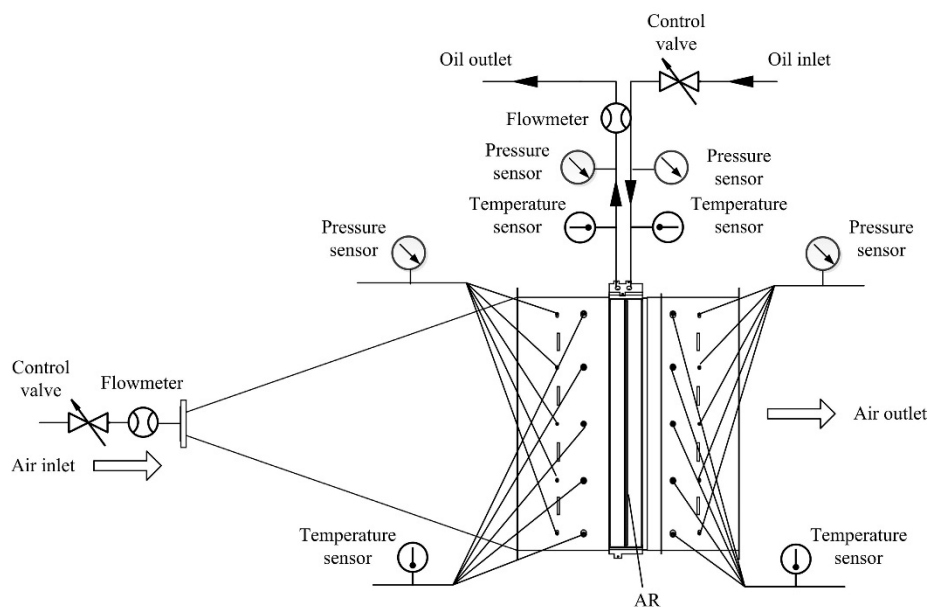


Figure 10. Experimental schematic diagram.

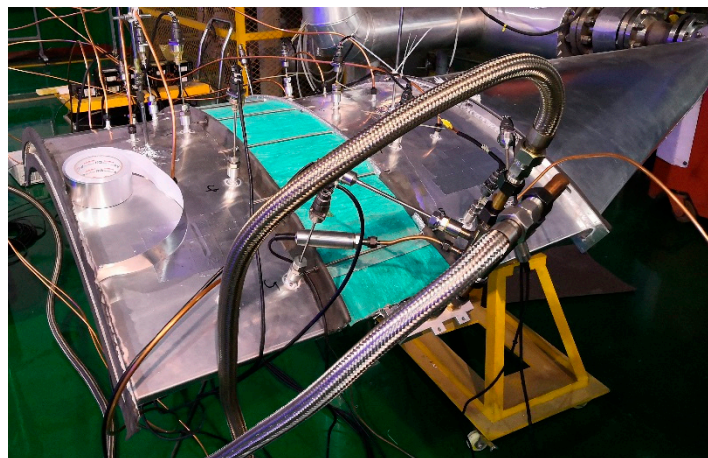
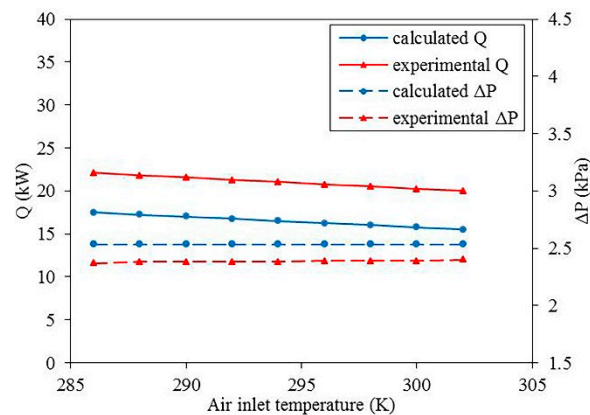


Figure 11. Testing equipment for AR.





**Figure 12.** Comparison between calculation results and experimental data.

As depicted in Figure 12,  $\Delta P$  obtained by this method was consistent with the experimental data, while the error of  $Q$  was higher than  $\Delta P$ . The deviations of  $Q$  and  $\Delta P$  were 20.7–22.4% and 5.5–6.9% with the average errors of 21.5% and 6.2%, respectively. The reason for this is that, as shown in Equation (3), half of  $\Delta P$  is directly obtained by CFD simulation, which is accurate. However, the calculation of  $Q$  using PFHX performance calculation formulas only can consider the heat transfer of the air that flows through the clearances of fins, while the air that flows above fins also participates in the heat transfer process. Even though the heat transfer effect of the air flowing above fins is very small, it can still influence the precision of  $Q$  calculation and make the calculated values by this method lower than the experimental data. Thus, if a highly accurate  $Q$  result is needed, this part of air also needs to be considered, which is not realizable through using PFHX theoretical formulae directly. AR needs to be emulated as a whole directly to meet the high accuracy requirement, which is too time-consuming to realize in engineering applications. In the design process of engineering applications, the precision of this method is enough for AR performance prediction, and it is more convenient and time saving. Hence, it can be concluded that this method is feasible for engineering applications, and can be used in the configuration optimization process in this research.

Ignoring factors of this method itself, there are also some other reasons that can cause the differences between the calculation results and the experimental data, just like deviations of formulas themselves, simplification of simulation model, and unavoidable experimental errors.

### 3.2. Design Parameter Effects and Configuration Optimization Results

#### 3.2.1. Functional Relationships Fitting

In this case, 16 sets of HTU simulation data under different values of FH and NFCD were averagely obtained within design parameter constraints, and the surfaces of fitting were obtained using least square method and polynomial fitting based on these data. The fitting surfaces are shown in Figures 13 and 14, and the functional relationships can be represented by Equations (7) and (8).

$$k = 0.03211 + 0.03009x - 0.0001297y + 0.0002819x^2 - 3.732 \times 10^{-5}xy + 4.445 \times 10^{-8}y^2 - 8.684 \times 10^{-6}x^3 + 1.589 \times 10^{-6}x^2y - 2.16 \times 10^{-8}xy^2 \quad (7)$$

$$\Delta P = -0.6039 + 0.1434x + 0.004469y - 0.009944x^2 - 0.000316xy - 1.103 \times 10^{-5}y^2 + 0.000389x^3 - 8.93 \times 10^{-6}x^2y + 1.378 \times 10^{-6}xy^2 \quad (8)$$

Sum of squares due to error (SSE) and the coefficient of determination  $R^2$  are significant goodness of fit criteria to evaluate the accuracy of fitting function [45]. The closer the SSE and  $R^2$  are to 0 and 1, respectively, the better is the fitting function. The SSEs of Equations (7) and (8) are  $1.9739 \times 10^{-5}$  and

0.0033, and the  $R^2$  values of that are 0.9999 and 0.9993, respectively. Hence, the functional relationships can be obtained accurately.

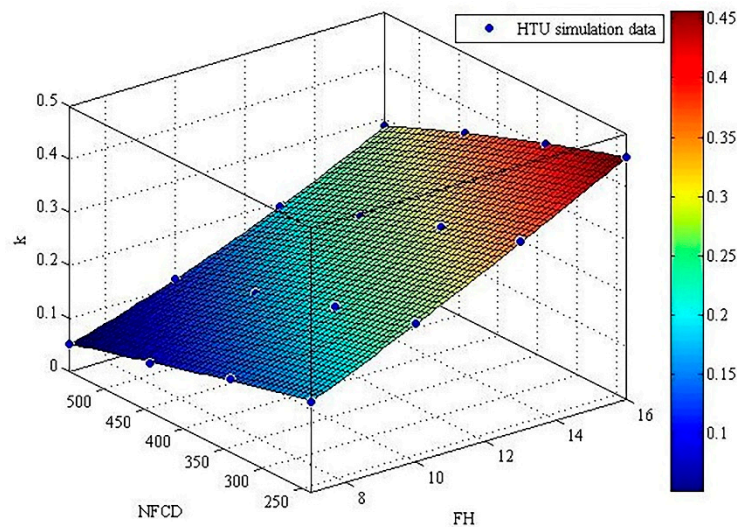


**Figure 13.** Fitting surface for the percentage of the air that can be calculated in PFHX performance calculation formulas ( $k$ ).

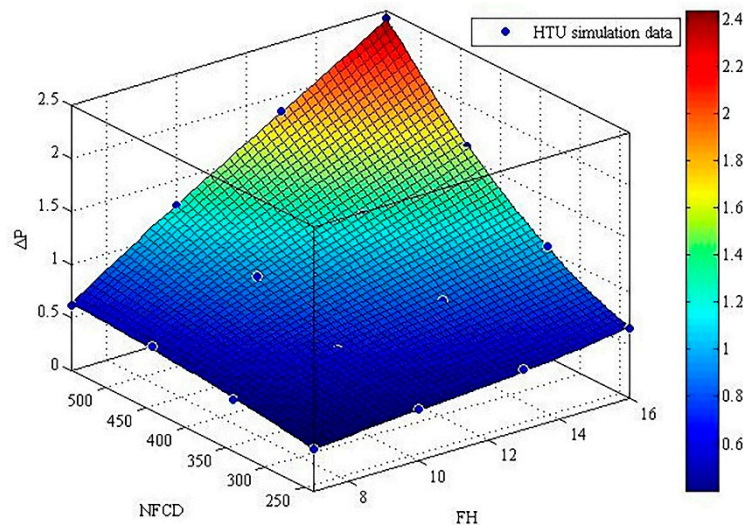


**Figure 14.** Fitting surface for air-side pressure drop of AR ( $\Delta P$ ).

### 3.2.2. Design Parameter Effects

The effects of design parameters on  $Q$  and  $\Delta P$  were analyzed based on Equations (7) and (8) and the AR performance calculation method. The effects of FH are represented in Figure 15, while NFCD was 544. As depicted, while FH increased from 7 mm to 16 mm,  $Q$  and  $\Delta P$  increased by 9.66–26.26 kW and 1.25–4.87 kPa, respectively. The growth of FH led to the increase of heat transfer area, which can lead to the increase of  $Q$ . At the same time, as FH rose, the influence area of fins rose, and the resistance influence of fins was enhanced. Thus,  $\Delta P$  increased continuously.

The effects of NFCD are shown in Figure 16, while FH was 10 mm. As depicted, while NFCD increased from 238 to 544,  $\Delta P$  increased by 0.96–2.53 kPa, and  $Q$  increased from 16.71 kW first, reaching its highest point of 19.77 kW when NFCD was 408, and then decreased to 17.25 kW. The increase of NFCD indicates the growth of the heat transfer area, which results in the increase of  $Q$  at first. Meanwhile the increase of NFCD can also lead to the decrease of the clearance space between two adjacent fins, which means that air is increasingly harder to flow through these clearances and the

velocity of air that flows through the air channel without fins increases. So,  $\Delta P$  increased continuously in this process, and  $k$  decreased continuously. The decrease of  $k$  will weaken the heat exchange capability of AR. After NFCD increases to a certain level, the decrease of  $k$  can lead to the decline of  $Q$ , even though heat transfer area is still increasing. Thus, the curve of  $Q$  rose first and then fell after the point.

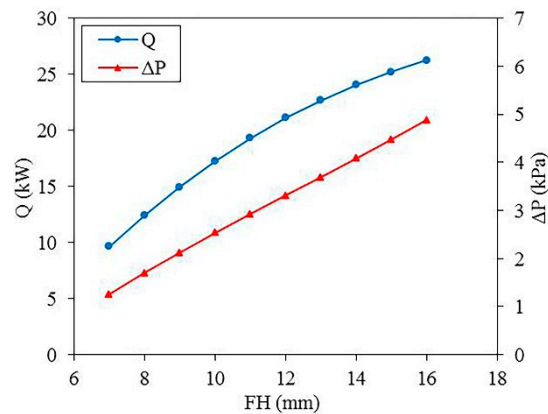


**Figure 15.** Heat transfer capacity ( $Q$ ) and  $\Delta P$  separately versus fin height (FH).

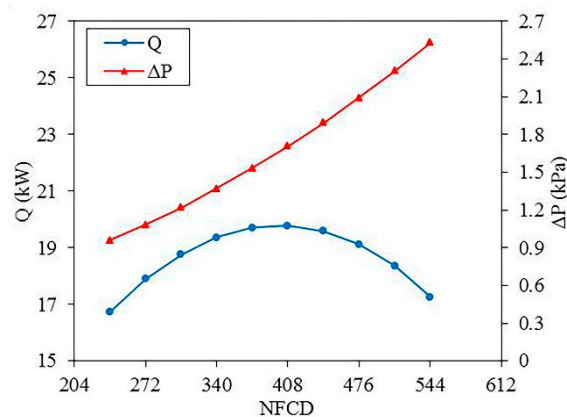


**Figure 16.**  $Q$  and  $\Delta P$  separately versus number of fins in circumferential direction (NFCD).

### 3.2.3. Optimization Results

In order to consider the comprehensive performance of AR, the multiobjective configuration optimization method driven by NSGA-II was conducted. The conflicting optimization objectives were set as the minimization of  $-Q$  and  $\Delta P$  both. Population size, maximum iteration number, analog binary cross distribution index, and polynomial mutation distribution index were set as 100, 500, 20, and 20, respectively. The obtained Pareto optimal points are shown in Figure 17.

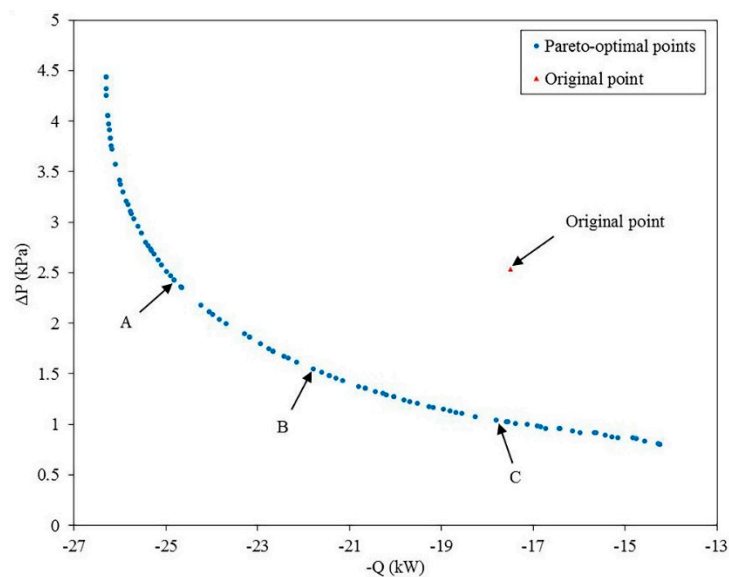


Figure 17. Pareto optimal points.

As depicted in Figure 17, both the values of  $-Q$  and  $\Delta P$  of some obtained optimal points were lower than that of the original point, which means that these obtained configurations had better comprehensive performances than the original one. In addition, three Pareto optimal solutions were chosen and are shown in Figure 17 and Table 3. The selection method of these three Pareto optimal solutions follows the following principles:

1.  $-Q$  of the point A is much lower than the original point, while  $\Delta P$  of it is only a little less than the original point.
2.  $-Q$  of the point C is only a little lower than the original point, while  $\Delta P$  of it is much less than the original point.
3. The point B is chosen from the points around the middle position in the range from the point A to the point C.

Table 3. Optimization performances comparison of AR.

Parameters	FH (mm)	NFCD	$Q$ (kW)	$\Delta P$ (kPa)
Original point	10	544	17.50	2.53
Optimal point A	16	375	24.81	2.42
Optimal point B	15	290	21.79	1.55
Optimal point C	11	248	17.79	1.04

Compared with the original point shown in Table 3,  $Q$  values of the point A, B, and C separately increased by 41.77%, 24.51%, and 1.66%, and  $\Delta P$  values of them decreased by 4.35%, 38.74%, and 58.89%, respectively. It is clearly shown that  $Q$  of the optimal configurations increased by 22.65% on average, while  $\Delta P$  decreased by 33.99% on average. Based on the above comparisons, it indicates that the proposed configuration optimization method is valid and feasible, and the comprehensive performance of AR can be enhanced by this method.

#### 4. Conclusions

In this research, a performance calculation method for AR was proposed and verified by experiment. Heat transfer capacity and air-side pressure drop were calculated through combining HTU simulation and PFHX performance calculation formulas, rather than through emulating AR as a whole directly. So, the problem of the huge amount of grids generated by meshing AR can be

effectively avoided, which means that this method is convenient to use and can save calculation time and computing resources. It demonstrates the feasibility of this performance calculation method for engineering applications.

Based on this performance calculation method, a configuration optimization method for AR was also come up with using NSGA-II in this research. Heat transfer capacity maximization and air-side pressure drop minimization were regarded as two conflicting objectives, and FH and NFCD were set as two design parameters. A set of Pareto optimal solutions were obtained and some of them had better comprehensive performances than the original configurations. Three optimal solutions were chosen and compared with the original configuration. The comparison results illustrate that the heat transfer capacity of the optimal configurations increased by 22.65% on average compared with the original configuration, while the air-side pressure drop decreased by 33.99% on average. It indicates that this configuration optimization method is valid and can provide a significant guidance for AR design.

**Author Contributions:** Conceptualization, Z.X.; investigation, Z.X. and H.M.; methodology, Z.X.; project administration, Y.G. and H.Y.; resources, Z.X. and Z.Y.; software, Z.X.; supervision, Y.G. and H.Y.; validation, Z.X.; visualization, Z.X.; writing—original draft, Z.X.; writing—review and editing, Z.X., Y.G., Z.Y., and R.L. All authors have read and agreed to the published version of the manuscript.

**Funding:** This research received no external funding.

**Conflicts of Interest:** The authors declare no conflict of interest.

## Nomenclature

### Latin letters

$A$	heat transfer area	$\text{m}^2$
$C^*$	heat capacity rate ratio	-
$c_p$	specific heat capacity	$\text{J}/(\text{kg}\cdot\text{K})$
$h$	wave height of fins	$\text{m}$
$NTU$	number of transfer units	-
$Pr$	Prandtl number	-
$Q$	heat transfer capacity	$\text{W}$
$q_m$	mass flow rate	$\text{kg/s}$
$q_v$	volume flow rate	$\text{L/min}$
$R_w$	wall thermal resistance	$\text{K/W}$
$T$	inlet temperature	$\text{K}$
$U$	total heat transfer coefficient	$\text{W}/(\text{m}^2\cdot\text{K})$
$W$	thermal capacity rate	$\text{W/K}$
$Z$	set of integer	-

### Greek letters

$\alpha$	heat transfer coefficient	$\text{W}/(\text{m}^2\cdot\text{K})$
$\delta$	thickness	$\text{m}$
$\Delta P$	pressure drop	$\text{Pa}$
$\eta$	heat transfer efficiency	-
$\eta_A$	surface efficiency of air-side	-
$\eta_{fA}$	fin efficiency of air-side	-
$\eta_{fL}$	fin efficiency of liquid-side	-
$\eta_L$	surface efficiency of liquid-side	-
$\omega$	mass flow rate per square meter	$\text{kg}/(\text{m}^2\cdot\text{s})$
$\lambda$	heat conductivity	$\text{W}/(\text{m}\cdot\text{K})$

### Subscripts

$A$	air
$f$	fins
$L$	liquid
$p$	division plate
$w$	wall

## Appendix A

The basic formula of heat transfer capacity calculation of PFHX is shown by Equation (A1) [46]:

$$Q = \eta W_{\min}(T_L - T_A). \quad (\text{A1})$$

As the numbers of air passes and liquid passes are 1 and 2, respectively,  $\eta$  is given by Equations (A2)–(A7) [47]:

$$\eta = \frac{\left(\frac{1-C^*\eta_i}{1-\eta_i}\right)^2 - 1}{\left(\frac{1-C^*\eta_i}{1-\eta_i}\right)^2 - C^*}, \quad (\text{A2})$$

$$\eta_i = 1 - \exp\left\{\frac{NTU^{0.22}}{C^*}[\exp(-C^*NTU^{0.78}) - 1]\right\} \quad (\text{A3})$$

$$NTU = \frac{UA}{W_{\min}} \quad (\text{A4})$$

$$C^* = \frac{W_{\min}}{W_{\max}} \quad (\text{A5})$$

$$\frac{1}{UA} = \frac{1}{\eta_L \alpha_L A_L} + R_w + \frac{1}{\eta_A \alpha_A A_A} \quad (\text{A6})$$

$$R_w = \frac{\delta_p}{\lambda_w A_p} \quad (\text{A7})$$

In Equation (A6),  $\eta_L$  and  $\eta_A$  reflect surface efficiencies of liquid-side and air-side, respectively, and  $A_L$  and  $A_A$  separately represent heat transfer areas of liquid-side and air-side. These variables can be calculated by Equations (A8)–(A15) [47,48]:

$$\eta_L = 1 - \frac{A_{fL}}{A_L}(1 - \eta_{fL}), \quad (\text{A8})$$

$$\eta_A = 1 - \frac{A_{fA}}{A_A}(1 - \eta_{fA}) \quad (\text{A9})$$

$$A_L = A_p + A_{fL} \quad (\text{A10})$$

$$A_A = A_p + A_{fA} \quad (\text{A11})$$

$$\eta_{fL} = \frac{\tanh(m_L h_L)}{m_L h_L} \quad (\text{A12})$$

$$\eta_{fA} = \frac{\tanh(m_A h_A)}{m_A h_A} \quad (\text{A13})$$

$$m_L = \sqrt{\frac{2\alpha_L}{\lambda_{fL} \delta_{fL}}} \quad (\text{A14})$$

$$m_A = \sqrt{\frac{2\alpha_A}{\lambda_{fA} \delta_{fA}}} \quad (\text{A15})$$

$W$  and  $\alpha$  refer to thermal capacity rate and heat transfer coefficient, respectively, and they are given by Equations (A16) and (A17) [46,48]:

$$W = \dot{m} c_p \quad (\text{A16})$$

$$\alpha = \frac{j \omega c_p}{Pr^{2/3}} \quad (\text{A17})$$



## References

1. Bayram, H.; Sevilgen, G. Numerical investigation of the effect of variable baffle spacing on the thermal performance of a Shell and tube heat Exchanger. *Energies* **2017**, *10*, 1156. [\[CrossRef\]](#)
2. Yi, L.; Lei, C.; Jinrong, Q. One Method to Design a Heat Exchanger for Equipment Cooling Water. In *25th International Conference on Nuclear Engineering*; American Society of Mechanical Engineers Digital Collection: Shanghai, China, 2017.
3. Abdelkader, B.A.; Jamil, M.A.; Zubair, S.M. Thermal-hydraulic characteristics of helical baffle shell-and-tube heat exchangers. *Heat Transf. Eng.* **2019**, 1–34. [\[CrossRef\]](#)
4. Abdelkader, B.A.; Zubair, S.M. The Effect of a Number of Baffles on the performance of Shell-and-Tube Heat Exchangers. *Heat Transf. Eng.* **2019**, *40*, 39–52. [\[CrossRef\]](#)
5. Pal, E.; Kumar, I.; Joshi, J.B.; Maheshwari, N. CFD simulations of shell-side flow in a shell-and-tube type heat exchanger with and without baffles. *Chem. Eng. Sci.* **2016**, *143*, 314–340. [\[CrossRef\]](#)
6. Du, J.; Wu, X.; Li, R.; Cheng, R. Numerical Simulation and Optimization of MID-Temperature Heat Pipe Exchanger. *Fluid Dyn. Mater. Process.* **2019**, *15*, 77–87. [\[CrossRef\]](#)
7. Ramadan, M.; Khaled, M.; Jaber, H.; Faraj, J.; Bazzi, H.; Lemenand, T. Numerical simulation of Multi-Tube Tank heat exchanger: Optimization analysis. *Energy Sour. Part A Recovery Util. Environ. Eff.* **2019**, 1–11. [\[CrossRef\]](#)
8. Yang, Y.; Hu, H.; Su, P.; Mei, X.; Sun, W. Characteristic Analysis and Structure Optimization of a Type of Plate Heat Exchanger. In *IOP Conference Series: Earth and Environmental Science*; IOP Publishing: Bristol, UK, 2019; p. 042055.
9. Raul, A.; Bhasme, B.; Maurya, R. A numerical investigation of fluid flow maldistribution in inlet header configuration of plate fin heat exchanger. *Energy Procedia* **2016**, *90*, 267–275. [\[CrossRef\]](#)
10. Cai, H.; Su, L.; Liao, Y.; Weng, Z. Numerical and experimental study on the influence of top bypass flow on the performance of plate fin heat exchanger. *Appl. Therm. Eng.* **2019**, *146*, 356–363. [\[CrossRef\]](#)
11. Shinde, S.; Hadgekar, P.; Pavithran, S. Comparative thermal analysis of helixchanger with segmental heat exchanger using bell-delaware method. *Int. J. Adv. Eng. Technol.* **2012**, *3*, 235.
12. El Maakoul, A.; Laknizi, A.; Saadeddine, S.; El Metoui, M.; Zaite, A.; Meziane, M.; Abdellah, A.B. Numerical comparison of shell-side performance for shell and tube heat exchangers with trefoil-hole, helical and segmental baffles. *Appl. Therm. Eng.* **2016**, *109*, 175–185. [\[CrossRef\]](#)
13. Wang, K.; Bai, C.; Wang, Y.; Liu, M. Flow dead zone analysis and structure optimization for the trefoil-baffle heat exchanger. *Int. J. Therm. Sci.* **2019**, *140*, 127–134. [\[CrossRef\]](#)
14. Wang, S.; Xiao, J.; Ye, S.; Song, C.; Wen, J. Numerical investigation on pre-heating of coal water slurry in shell-and-tube heat exchangers with fold helical baffles. *Int. J. Heat Mass Transf.* **2018**, *126*, 1347–1355. [\[CrossRef\]](#)
15. Amini, R.; Amini, M.; Jafarinia, A.; Kashfi, M. Numerical investigation on effects of using segmented and helical tube fins on thermal performance and efficiency of a shell and tube heat exchanger. *Appl. Therm. Eng.* **2018**, *138*, 750–760. [\[CrossRef\]](#)
16. Godino, D.M.; Corzo, S.F.; Nigro, N.M.; Ramajo, D.E. CFD simulation of the pre-heater of a nuclear facility steam generator using a thermal coupled model. *Nucl. Eng. Des.* **2018**, *335*, 265–278. [\[CrossRef\]](#)
17. Gu, X.; Zheng, Z.; Xiong, X.; Wang, T.; Luo, Y.; Wang, K. Characteristics of Fluid Flow and Heat Transfer in the Shell Side of the Trapezoidal-like Tilted Baffles Heat Exchanger. *J. Therm. Sci.* **2018**, *27*, 602–610. [\[CrossRef\]](#)
18. Milcheva, I.; Heberle, F.; Brüggemann, D. Modeling and simulation of a shell-and-tube heat exchanger for Organic Rankine Cycle systems with double-segmental baffles by adapting the Bell-Delaware method. *Appl. Therm. Eng.* **2017**, *126*, 507–517. [\[CrossRef\]](#)
19. Sanaye, S.; Hajabdollahi, H. Multi-objective optimization of shell and tube heat exchangers. *Appl. Therm. Eng.* **2010**, *30*, 1937–1945. [\[CrossRef\]](#)
20. Chahartaghi, M.; Eslami, P.; Naminezhad, A. Effectiveness improvement and optimization of shell-and-tube heat exchanger with entransy method. *Heat Mass Transf.* **2018**, *54*, 3771–3784. [\[CrossRef\]](#)
21. Xu, Z.; Guo, Y.; Mao, H.; Yang, F. Configuration Optimization and Performance Comparison of STHX-DDB and STHX-SB by A Multi-Objective Genetic Algorithm. *Energies* **2019**, *12*, 1794. [\[CrossRef\]](#)
22. Song, R.; Cui, M. Single-and multi-objective optimization of a plate-fin heat exchanger with offset strip fins adopting the genetic algorithm. *Appl. Therm. Eng.* **2019**, *159*, 113881. [\[CrossRef\]](#)

23. Wen, J.; Gu, X.; Wang, M.; Wang, S.; Tu, J. Numerical investigation on the multi-objective optimization of a shell-and-tube heat exchanger with helical baffles. *Int. Commun. Heat Mass Transf.* **2017**, *89*, 91–97. [\[CrossRef\]](#)
24. Wang, S.; Xiao, J.; Wang, J.; Jian, G.; Wen, J.; Zhang, Z. Configuration optimization of shell-and-tube heat exchangers with helical baffles using multi-objective genetic algorithm based on fluid-structure interaction. *Int. Commun. Heat Mass Transf.* **2017**, *85*, 62–69. [\[CrossRef\]](#)
25. Wang, S.; Xiao, J.; Wang, J.; Jian, G.; Wen, J.; Zhang, Z. Application of response surface method and multi-objective genetic algorithm to configuration optimization of Shell-and-tube heat exchanger with fold helical baffles. *Appl. Therm. Eng.* **2018**, *129*, 512–520. [\[CrossRef\]](#)
26. Wang, S.; Jian, G.; Xiao, J.; Wen, J.; Zhang, Z.; Tu, J. Fluid-thermal-structural analysis and structural optimization of spiral-wound heat exchanger. *Int. Commun. Heat Mass Transf.* **2018**, *95*, 42–52. [\[CrossRef\]](#)
27. Wang, G.; Wang, D.; Deng, J.; Lyu, Y.; Pei, Y.; Xiang, S. Experimental and numerical study on the heat transfer and flow characteristics in shell side of helically coiled tube heat exchanger based on multi-objective optimization. *Int. J. Heat Mass Transf.* **2019**, *137*, 349–364. [\[CrossRef\]](#)
28. Gu, X.; Wang, T.; Chen, W.; Luo, Y.; Tao, Z. Multi-objective Optimization on Structural Parameters of Torsional Flow Heat Exchanger. *Appl. Therm. Eng.* **2019**, *161*, 113831. [\[CrossRef\]](#)
29. Amanuel, T.; Mishra, M. Thermohydraulic optimization of triple concentric-tube heat exchanger: A multi-objective approach. *Proc. Inst. Mech. Eng. Part E J. Process Mech. Eng.* **2019**, *233*, 589–600. [\[CrossRef\]](#)
30. Mohanty, D.K. Application of firefly algorithm for design optimization of a shell and tube heat exchanger from economic point of view. *Int. J. Therm. Sci.* **2016**, *102*, 228–238. [\[CrossRef\]](#)
31. De Vasconcelos Segundo, E.H.; Amoroso, A.L.; Mariani, V.C.; Dos Santos Coelho, L. Economic optimization design for shell-and-tube heat exchangers by a Tsallis differential evolution. *Appl. Therm. Eng.* **2017**, *111*, 143–151. [\[CrossRef\]](#)
32. Tharakeshwar, T.; Seetharamu, K.; Prasad, B.D. Multi-objective optimization using bat algorithm for shell and tube heat exchangers. *Appl. Therm. Eng.* **2017**, *110*, 1029–1038. [\[CrossRef\]](#)
33. Etghani, M.M.; Baboli, S.A.H. Numerical investigation and optimization of heat transfer and exergy loss in shell and helical tube heat exchanger. *Appl. Therm. Eng.* **2017**, *121*, 294–301. [\[CrossRef\]](#)
34. Esfe, M.H.; Mahian, O.; Hajmohammad, M.H.; Wongwises, S. Design of a heat exchanger working with organic nanofluids using multi-objective particle swarm optimization algorithm and response surface method. *Int. J. Heat Mass Transf.* **2018**, *119*, 922–930. [\[CrossRef\]](#)
35. Dhavle, S.V.; Kulkarni, A.J.; Shastri, A.; Kale, I.R. Design and economic optimization of shell-and-tube heat exchanger using cohort intelligence algorithm. *Neural Comput. Appl.* **2018**, *30*, 111–125. [\[CrossRef\]](#)
36. Hao, J.-H.; Chen, Q.; Ren, J.-X.; Zhang, M.-Q.; Ai, J. An experimental study on the offset-strip fin geometry optimization of a plate-fin heat exchanger based on the heat current model. *Appl. Therm. Eng.* **2019**, *154*, 111–119. [\[CrossRef\]](#)
37. Chien, N.B.; Linh, N.X.; Jong-Taek, O. Numerical Optimization of Flow Distribution inside Inlet Header of Heat Exchanger. *Energy Procedia* **2019**, *158*, 5488–5493. [\[CrossRef\]](#)
38. Kumar, S.D.; Chandramohan, D.; Purushothaman, K.; Sathish, T. Optimal hydraulic and thermal constrain for plate heat exchanger using multi objective wale optimization. *Mater. Today: Proc.* **2019**. [\[CrossRef\]](#)
39. Kobayashi, H.; Yaji, K.; Yamasaki, S.; Fujita, K. Freeform winglet design of fin-and-tube heat exchangers guided by topology optimization. *Appl. Therm. Eng.* **2019**, *161*, 114020. [\[CrossRef\]](#)
40. More, K.C.; Rao, R.V. Design Optimization of Plate-Fin Heat Exchanger by Using Modified Jaya Algorithm. In *Advanced Engineering Optimization through Intelligent Techniques*; Springer: Berlin/Heidelberg, Germany, 2020; pp. 165–172.
41. Ansys Inc. *ANSYS Fluent User's Guide*; ANSYS: Canonsburg, PA, USA, 2018.
42. Yue, S.; Wang, Y.; Wang, H. Design and optimization of tandem arranged cascade in a transonic compressor. *J. Therm. Sci.* **2018**, *27*, 349–358. [\[CrossRef\]](#)
43. Deb, K.; Pratap, A.; Agarwal, S.; Meyarivan, T. A fast and elitist multiobjective genetic algorithm: NSGA-II. *IEEE Trans. Evol. Comput.* **2002**, *6*, 182–197. [\[CrossRef\]](#)
44. Wen, J.; Yang, H.; Tong, X.; Li, K.; Wang, S.; Li, Y. Optimization investigation on configuration parameters of serrated fin in plate-fin heat exchanger using genetic algorithm. *Int. J. Therm. Sci.* **2016**, *101*, 116–125. [\[CrossRef\]](#)

45. Renaud, O.; Victoria-Feser, M.-P. A robust coefficient of determination for regression. *J. Stat. Plan. Inference* **2010**, *140*, 1852–1862. [[CrossRef](#)]
46. Shah, R.K.; Sekulic, D.P. *Fundamentals of Heat Exchanger Design*; John Wiley & Sons: Hoboken, NJ, USA, 2003.
47. Yu, J. *Heat Exchanger Principle and Design*; Beijing University of Aeronautics and Astronautics Press: Beijing, China, 2006.
48. Qi, M. *Refrigeration Accessories*; Aviation Industry Press: Beijing, China, 1992.



© 2020 by the authors. Licensee MDPI, Basel, Switzerland. This article is an open access article distributed under the terms and conditions of the Creative Commons Attribution (CC BY) license (<http://creativecommons.org/licenses/by/4.0/>).